Journal Pre-proof



Engineering a synergistic ultrathin g-C_3N_4 nanotube–MgO(200) system that drives efficient PMS activation for the selective conversion of organophosphorus pesticides into inorganic phosphates

Yifei Wang, Yiwei He, Sihui Yang, Jiayi Yuan, Guojing Wang, Xiaoyu Zhang, Pengfei Cheng, Artem Yurevich Manyakhin, Xiaolin Xu, Jianhua Fan, Yanyan Dang, Xiongfang An

PII: S2950-1555(26)00125-4

DOI: https://doi.org/10.1016/j.greenca.2026.06.009

Reference: GREENC245

To appear in: *Green Carbon*

Received date: 13 March 2026
Revised date: 18 May 2026
Accepted date: 21 June 2026

Please cite this article as: Yifei Wang, Yiwei He, Sihui Yang, Jiayi Yuan, Guojing Wang, Xiaoyu Zhang, Pengfei Cheng, Artem Yurevich Manyakhin, Xiaolin Xu, Jianhua Fan, Yanyan Dang and Xiongfang An, Engineering a synergistic ultrathin g-C_3N_4 nanotube–MgO(200) system that drives efficient PMS activation for the selective conversion of organophosphorus pesticides into inorganic phosphates, *Green Carbon,* (2026) doi:https://doi.org/10.1016/j.greenca.2026.06.009

This is a PDF of an article that has undergone enhancements after acceptance, such as the addition of a cover page and metadata, and formatting for readability. This version will undergo additional copyediting, typesetting and review before it is published in its final form. As such, this version is no longer the Accepted Manuscript, but it is not yet the definitive Version of Record; we are providing this early version to give early visibility of the article. Please note that Elsevier's sharing policy for the Published Journal Article applies to this version, see: https://www.elsevier.com/about/policies-and-standards/sharing#4-published-journal-article. Please also note that, during the production process, errors may be

discovered which could affect the content, and all legal disclaimers that apply to the journal pertain.

© 2026 Published by Elsevier.

Engineering a synergistic ultrathin g-C_3N_4 nanotube–MgO(200) system that drives efficient PMS activation for the selective conversion of organophosphorus pesticides into inorganic phosphates

Yifei Wang [a1], Yiwei He [a1], Sihui Yang [a], Jiayi Yuan [a], Guojing Wang [a], Xiaoyu Zhang [a], Pengfei Cheng [b], Artem Yurevich Manyakhin [c], Xiaolin Xu [a], Jianhua Fan [a], Yanyan Dang [a*], Xiongfang An [a*]

[a] School of Chemistry and Chemical Engineering, Shihezi University, Shihezi, 832003 China

[b] College of Food Science and Engineering, Ningbo University, Ningbo, Zhejiang 315211, PR China

[c] Federal Scientific Center of the East Asia Terrestrial Biodiversity, Far Eastern Branch, Russian Academy of Sciences, Vladivostok 690022, PR Russia

* Corresponding author.

Xiongfang An, Tel: 0993-2057272, Email address: shz_anxiongf@163.com

Yanyan Dang, Tel: 0993-2057272, Email address: dyyshz@126.com

Journal Pre-proof

ABSTRACT

The treatment of organophosphorus pesticide (OP) wastewater and the recovery of inorganic phosphate (IP) resources are constrained by traditional technological bottlenecks. The core challenge lies in achieving both efficient degradation of OPs and simultaneous recovery of IPs within a single system. In this study, a bifunctional MgO(200)@g-C_3N_4 composite catalyst was prepared via hydrothermal synthesis to activate peroxymonosulfate (PMS), degrade OPs (e.g., glyphosate), and selectively adsorb IPs. The system demonstrated robust performance, rapidly converting glyphosate into recoverable IPs. Even in complex aqueous matrices, this system delivered exceptional stability and catalytic performance, affording 87.9% glyphosate degradation within 40 min at an initial glyphosate concentration of 10 mg/L, alongside a high inorganic phosphate recovery of 84.3%. Moreover, the IP fertilizer recovered from simulated wastewater in a continuous-flow reactor exhibited excellent growth-promoting effects on crops in agricultural validation tests. Mechanistic studies revealed that ultrathin g-C_3N_4 nanotubes act as an electron-transfer medium, mediating electron transfer between glyphosate and PMS and activating PMS to generate reactive species composed mainly of $SO_4^{\bullet-}$ and $\bullet O_2^-$, which convert glyphosate into IPs. Meanwhile, the high-density Mg^{2+} ions exposed on the (200) crystal plane of MgO can form stable magnesium phosphate precipitates with the IPs generated during degradation. This technology enables the continuous degradation of OPs while simultaneously adsorbing and immobilizing IPs, thereby transforming pollutants into potential nutrients and mitigating aquatic toxicity.

Journal Pre-proof

Keywords: Organophosphorus wastewater; Photodegradation; PMS activation; Directed transformation; Phosphorus recovery;

Journal Pre-proof

1. Introduction

The treatment of phosphorus-containing wastewater remains a major challenge for water pollution control. Due to their wide use and high residual properties, organophosphorus pesticides (OPs), represented by glyphosate, have become the main source of persistent OP pollution in water bodies[1]. The intermediate products generated during the degradation of these pollutants in the natural environment or through traditional treatment processes, such as the toxic aminomethylphosphonic acid (AMPA), and the final mineralization products, inorganic phosphates (IPs) (e.g., PO_4^{3-}), can cause secondary pollution and trigger the eutrophication of water bodies[2,3]. However, traditional treatment technologies often focus on the degradation of the parent compounds of OPs and neglect the secondary pollution caused by IPs[4]. Therefore, achieving efficient and complete degradation of high-stability OPs (e.g., glyphosate) and simultaneously capturing and recycling the generated IPs have become core challenges in the current coordinated development of wastewater treatment and resource recovery[5].

For the removal of OPs, advanced oxidation processes (AOPs) based on the activation of peroxymonosulfate (PMS) to generate strong oxidizing reactive species have shown significant advantages[6,7]. This technology can produce various reactive species, such as hydroxyl radicals (•OH), sulfate radicals ($SO_4^{\bullet-}$), superoxide radicals ($\bullet O_2^-$), and singlet oxygen ($^1O_2$), achieving efficient degradation of pollutants[8–10]. Among numerous catalytic materials, g-C_3N_4 catalysts have attracted significant attention for PMS activation because of their unique visible-light response and suitable

band structure[11,12]. By constructing ultrathin nanotube structures, the electronic structure can be further regulated, increasing the exposure of active sites and promoting carrier separation and interfacial electron transfer, thereby significantly enhancing the activation efficiency of PMS. Nevertheless, while effectively degrading OPs, this system also mineralizes them into soluble IPs, leading to the persistent presence of phosphates in water bodies and posing risks of secondary pollution and eutrophication. Despite recent advances in PMS-driven AOPs for OP mineralization, most systems still suffer from insufficient in situ phosphate capture and a lack of synergistic design between catalytic oxidation and adsorption recovery[13,14]. Therefore, achieving the simultaneous removal and recovery of IPs during the degradation of OPs has become a key challenge for the practical application of this technology.

To address this issue, bifunctional catalytic-adsorptive materials that can achieve OP degradation and phosphate immobilization in a single step have been rapidly developed over the past two years[15]. In response to the demand for the deep removal of IPs generated from OP mineralization, magnesium oxide (MgO) has demonstrated excellent IP adsorption potential because of its high theoretical adsorption capacity, environmental friendliness, and abundant surface magnesium sites[16,17]. Among its crystal planes, the MgO(200) crystal plane, with its high surface energy and high density of exposed Mg^{2+} sites, exhibits a strong affinity for PO_4^{3-}[18,19]. Compared to traditional adsorption materials, MgO(200) not only has a high adsorption capacity and rapid kinetics but also provides an ideal platform for the deep removal of low-concentration IPs[20,21]. However, this material faces challenges such as poor

selectivity, difficult recovery, and pH sensitivity in practical water applications, which restrict its large-scale application. Although g-C_3N_4 and MgO have both shown excellent performance in their respective fields, the approach of simply physically mixing the two still faces significant challenges: PMS activation needs to be carried out under slightly acidic conditions, whereas MgO adsorption is more suitable in neutral and weakly alkaline environments, and the mismatch of pH ranges severely restricts the synergistic effect. In addition, coexisting components in complex water bodies are prone to competing for free radicals and adsorption sites, causing a dual decline in catalytic and adsorption performance. More importantly, the heterogeneous structure with poor interfacial contact eterogeneous structure may lead to increased interfacial mass-transfer resistance or even functional inhibition[22].

Therefore, in this study, we designed and constructed an integrated composite catalyst, MgO(200)@g-C_3N_4, to synergistically couple PMS activation and IP capture. This material not only utilizes g-C_3N_4 to promote electron transfer and enhance PMS activation efficiency, but also takes advantage of MgO(200) to achieve in situ phosphorus fixation. When OPs are catalytically mineralized on the surface of g-C_3N_4 to generate IPs, they are rapidly captured by the high-density Mg^{2+} sites on the adjacent MgO(200) surface, forming stable IP precipitates and effectively avoiding secondary pollution. This tightly coupled degradation–adsorption synergistic mechanism simultaneously achieves efficient removal of OPs and stable recovery of IP resources within a single system, providing a novel material solution for the comprehensive treatment and resource recovery of OP-containing wastewater.

2. Materials and Methods

2.1. Chemicals

Melamine ($C_3H_6N_6$, CAS 108-78-1, 99% purity), cyanuric acid ($C_3H_3N_3O_3$, CAS 108-80-5, 99% purity), magnesium carbonate ($MgCO_3$, CAS 546-93-0, 40–47% purity), and potassium peroxymonosulfate ($KHSO_5$, CAS 10058-23-8, 98% purity) were purchased from Macklin Biochemical Co., Ltd. (Shanghai, China). HPLC-grade acetonitrile (C_2H_3N; CAS 75-05-8) and methanol (CH_3OH; CAS 67-56-1) were obtained from Merck KGaA (Darmstadt, Germany). Glyphosate, an herbicide, was selected as the target pollutant to evaluate the photocatalytic performance of the catalysts. Scavenging agents, including ethanol (EtOH), 1,4-benzoquinone (BQ), *tert*-butanol (TBA), and furfuryl alcohol (FFA), were sourced from Sigma-Aldrich and used to identify the reactive species.

2.2. Synthesis of tubular g-C_3N_4 and MgO(200)@g-C_3N_4 catalysts.

g-C_3N_4 nanotubes were fabricated via a supramolecular assembly method: equimolar melamine and cyanuric acid were separately dissolved in deionized water at 80 °C. The melamine solution was added dropwise into the cyanuric acid solution under continuous stirring to induce self-assembly. The product was collected by centrifugation, washed with hot deionized water at 80 °C, freeze-dried to obtain the precursor, and finally calcined at 520 °C for 2 h under Ar with a heating rate of 2 °C·min^{-1}.

The MgO(200)@g-C_3N_4 composite was synthesized using an ultrasound-assisted method. g-C_3N_4 was dispersed in methanol, followed by the addition of MgO

nanoparticles at a mass ratio of MgO to g-C_3N_4 of 1:5. After magnetic stirring, ultrasonic homogenization, drying, and grinding, the mixture was calcined under Ar to yield the final product.

2.3. Characterizations

The detailed experimental procedures for material characterization are provided in the **Supplementary Materials**.

2.4. Photocatalytic activity tests

The experimental procedures for the catalytic and adsorption studies, as well as for the actual wastewater treatment, are described in the **Supplementary Materials**.

3. Results and Discussion

3.1 Structure and morphology of the photocatalyst

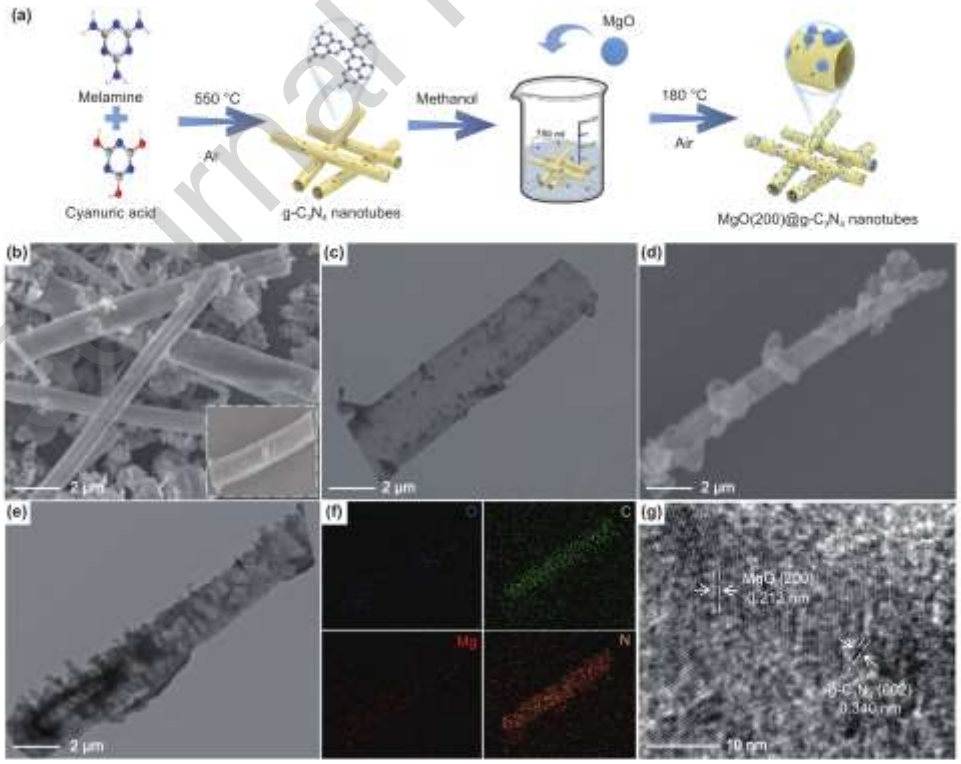


Fig. 1. (a) Schematic illustration of the formation of MgO(200)@g-C_3N_4 nanotube composites; (b) SEM image of g-C_3N_4; (c) TEM image of g-C_3N_4; (d) SEM image of MgO(200)@g-C_3N_4; (e) TEM image of MgO(200)@g-C_3N_4; (f) elemental mapping

images for N, Mg, C, and O within MgO(200)@g-C_3N_4; (g) HRTEM image of MgO(200)@g-C_3N_4.

A self-assembly strategy and an ultrasonication-assisted approach were adopted to construct the MgO(200)@g-C_3N_4 composites; the synthesis scheme is illustrated in **Fig. 1(a)**. First, melamine and cyanuric acid formed carbon nitride precursors through intermolecular hydrogen bonds (such as –NH···O and –NH···N) and self-assembled at low temperatures. Subsequently, the carbon nitride precursors were annealed to obtain carbon nitride nanotubes. Finally, MgO was loaded onto the carbon nitride nanotubes via calcination. The morphology and microstructure of MgO(200)@g-C_3N_4 were examined by scanning electron microscopy (SEM) and transmission electron microscopy (TEM). As shown in **Fig. 1(b)**, the pristine g-C_3N_4 nanotubes exhibit a uniform tubular morphology with smooth surfaces. TEM analysis further reveals the hollow nanotube architecture of g-C_3N_4 with a diameter in the range of 300–600 nm and lengths of 10–15 μm (**Fig. 1(c)**). **Fig. 1(d)** displays the SEM image of MgO(200)@g-C_3N_4. Disordered MgO nanoparticles with a size of 40–100 nm are non-uniformly distributed on the g-C_3N_4 nanotube. Similarly, the TEM images show that the g-C_3N_4 nanotube with grown MgO particles (**Fig. 1(e)**) is much rougher than the pristine g-C_3N_4 nanotube (**Fig. 1(c)**). Elemental mapping of MgO(200)@g-C_3N_4 (**Fig. 1(f)**) verifies the homogeneous distribution of N and C, while O and Mg exhibit a discrete and non-uniform distribution. This finding confirms that MgO does not coat the surface of g-C_3N_4 uniformly; instead, it exists as discrete nanoparticles. The HRTEM image of MgO(200)@g-C_3N_4 is shown in **Fig. 1(g)**; the lattice spacings corresponding to the (200) plane of MgO and the (220) plane of g-C_3N_4 are 0.213 nm

and 0.340 nm, respectively.

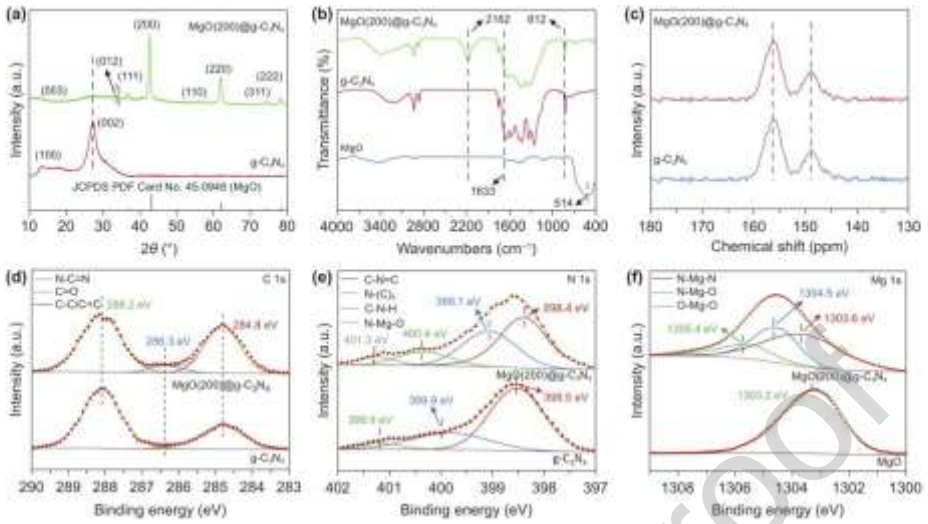


Fig. 2. (a) XRD patterns for g-C_3N_4 and MgO(200)@g-C_3N_4; (b) FTIR spectra of g-C_3N_4, MgO, and MgO(200)@g-C_3N_4; (c) ^{13}C solid-state NMR spectra of g-C_3N_4 and MgO(200)@g-C_3N_4; (d) XPS spectra of C 1s electrons for g-C_3N_4 and MgO(200)@g-C_3N_4; (e) XPS spectra of N 1s electrons for g-C_3N_4 and MgO(200)@g-C_3N_4; (f) XPS spectra of Mg 1s electrons for MgO and MgO(200)@g-C_3N_4.

The crystalline phase structures of the MgO, g-C_3N_4 and MgO(200)@g-C_3N_4 samples were investigated using X-ray diffraction (XRD). As shown in **Fig. 2(a)**, the XRD pattern of g-C_3N_4 exhibits two characteristic diffraction peaks at 13.0° and 27.4°, which correspond to the (100) and (002) crystal planes, respectively (JCPDS card No. 87-1526)[23]. Diffraction peaks for MgO are observed at 37.0°, 42.9°, 62.3°, 74.7°, and 78.7°, which correspond to the (111), (200), (220), (311), and (222) planes, respectively (JCPDS No. 45-0946)[24]. In addition to the MgO diffraction peaks, characteristic diffraction peaks at 18.9°, 34.1°, and 56.3° corresponding to the (003), (012), and (110) planes of rhombohedral MgNCN (JCPDS No. 00-051-0540), respectively, are detected[25]. During high-temperature calcination under Ar, g-C_3N_4 undergoes slight thermal decomposition to generate symmetric carbodiimide anions $[N=C=N]^{2-}$, which

further react with MgO via an in situ solid-phase coordination reaction to form the rhombohedral MgNCN crystal phase. The Fourier transform infrared (FTIR) spectra (**Fig. 2(b)**) reveal interfacial interactions in MgO(200)@g-C_3N_4. The composite shows new peaks at 2162 and 812 cm^{-1}, assigned to $[NCN]^{2-}$ stretching and deformation vibrations[25], alongside significantly attenuated characteristic peaks of g-C_3N_4 (1200–1700 cm^{-1}, C=N and C–N heterocycles)[26]. This attenuation confirms the successful interaction between MgO and g-C_3N_4. ^{13}C solid-state NMR spectra (**Fig. 2(c)**) reveal an unchanged carbon framework in MgO(200)@g-C_3N_4, which is consistent with the surface loading of MgO via physical adsorption or C–O–Mg bonds without altering the g-C_3N_4 core structure[12].

X-ray photoelectron spectroscopy (XPS) was used to confirm the surface compositions of the catalysts. The survey spectra (**Fig. S1**) identify C, N, O, and Mg in the MgO(200)@g-C_3N_4 composite, confirming the successful loading of MgO[27]. Furthermore, **Fig. 2(d)** shows that the C 1s peaks of g-C_3N_4 and MgO(200)@g-C_3N_4 appear at 288.2 and 284.8 eV, which are attributed to the N–C=N and C–C/C=C bonds, respectively[28]. Additionally, the peak at 286.3 eV is ascribed to the formation of C–O bonds between g-C_3N_4 and MgO[29]. The N 1s XPS spectrum of MgO(200)@g-C_3N_4 (**Fig. 2(e)**) shows three characteristic peaks at 398.4, 399.1, and 400.4 eV, which are ascribed to hybridized nitrogen (C–N=C), tertiary nitrogen (N–$(C)_3$), and amino functional groups (C–N–H)[30]. The peak at 401.3 eV corresponds to Mg–N bonding[24]. The catalytic activity of MgO(200)@g-C_3N_4 stems from its nitrogen-rich structure. In the C 1s spectrum (**Fig. 2(d)**), the carbon in the N–C=N configuration

(284.8 eV), which features a π-conjugated structure, can participate in electron transfer[31]. In the N 1s spectrum, the peak at 398.4 eV (**Fig. 2(e)**) is assigned to pyridinic nitrogen (C–N=C), and the lone pair of electrons on this nitrogen atom can trigger the oxidation of glyphosate[12]. Therefore, the N–C=N and C–N=C moieties are predicted to be the characteristic catalytic sites in MgO(200)@g-C_3N_4. Compared to that of pure MgO, the Mg 1s spectrum of the composite (**Fig. 2(f)**) shows two new peaks attributable to the formation of N–Mg–N (1303.6 eV) and N–Mg–O (1304.5 eV) bonds at the MgO/g-C_3N_4 interface[22]. In addition, the peak at 1305.4 eV corresponds to the O–Mg–O bond[25]. The adsorption capability stems from the interaction between MgO and phosphate (PO_4^{3-}). The formation of magnesium IP species (e.g., $Mg_3(PO_4)_2$) alters the local electronic environment of Mg, which manifests as a shift in the Mg 1s peak to a higher binding energy, confirming that the N–Mg–O and Mg–O sites serve as primary adsorption centers.

3.2. Optical and photoelectrochemical properties

Journal Pre-proof

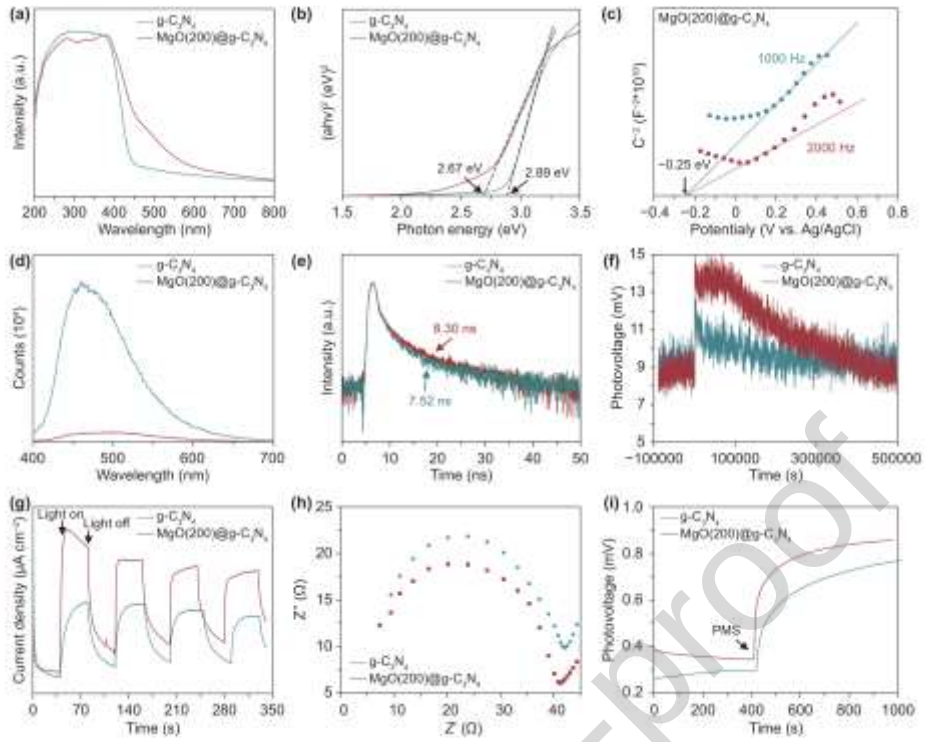


Fig. 3. (a) UV–vis diffuse reflectance spectra of g-C_3N_4 and MgO(200)@g-C_3N_4; (b) corresponding Tauc plot; (c) Mott–Schottky plot of MgO(200)@g-C_3N_4 at 1000 and 2000 Hz; (d) PL spectra of g-C_3N_4 and MgO(200)@g-C_3N_4; (e) time-resolved PL spectra of g-C_3N_4 and MgO(200)@g-C_3N_4; (f) TS-SPV spectra of g-C_3N_4 and MgO(200)@g-C_3N_4; (g) photocurrent responses for g-C_3N_4 and MgO(200)@g-C_3N_4; (h) electrochemical impedance spectra of g-C_3N_4 and MgO(200)@g-C_3N_4; (i) open-circuit potential plot for g-C_3N_4 and MgO(200)@g-C_3N_4.

UV–vis diffuse reflectance spectra and Mott-Schottky plots were collected to determine the energy-band structures of the synthesized photocatalysts[32,33]. The UV–vis absorption spectra (**Fig. 3(a)**) reveal that MgO(200)@g-C_3N_4 exhibits enhanced absorption in the visible-light region compared to pristine g-C_3N_4. According to the Kubelka–Munk theory, the estimated band gaps of g-C_3N_4 and MgO(200)@g-C_3N_4 are approximately 2.67 and 2.89 eV (**Fig. 3(b)**). Mott-Schottky measurements were used to determine that the flat-band potentials (vs. NHE) of g-C_3N_4 (**Fig. S2a**) and MgO(200)@g-C_3N_4 (**Fig. 3(c)**) are +0.067 V and -0.053 V, respectively. The corresponding band structure diagrams (**Fig. S2b**) demonstrate that MgO doping

Journal Pre-proof

induces a negative shift in the conduction band of MgO(200)@g-C_3N_4, which is thermodynamically more favorable than pristine g-C_3N_4 for activating PMS to generate reactive oxygen species.

The efficiency of the separation and migration of photogenerated carriers is crucial for achieving exceptional photocatalytic performance. To probe the separation efficiency of the photogenerated electron–hole pairs, PL tests were conducted on both g-C_3N_4 and MgO(200)@g-C_3N_4[34]. As shown in **Fig. 3(d)**, g-C_3N_4 exhibits a sharp emission peak at 463 nm. The PL intensity of MgO(200)@g-C_3N_4 decreases significantly, indicating a distinctly decreased number of singlet excitons. Time-resolved photoluminescence tests were performed to study the fluorescence lifetime of MgO(200)@g-C_3N_4 (**Fig. 3(e)**). The average lifetimes of the photogenerated carriers are listed in **Table 1**[35]. The average lifetime of MgO(200)@g-C_3N_4 (8.30 ns) is significantly longer than that of g-C_3N_4 (7.52 ns), suggesting an improved utilization efficiency of the photogenerated carriers. The transient surface photovoltage (TS-SPV) measurements (**Fig. 3(f)**) reveal a positive signal, indicating the migration of photogenerated holes to the catalyst surface[30]. The MgO(200)@g-C_3N_4 composite exhibits a significantly stronger photovoltage response than g-C_3N_4, directly demonstrating its superior electron–hole separation and charge-transport efficiency.

To further confirm the effective separation and transfer of the photoinduced charge carriers, the prepared catalysts were evaluated by electrochemical measurements. The MgO(200)@g-C_3N_4 composite exhibits a higher photocurrent density than g-C_3N_4 in transient photocurrent tests (**Fig. 3(g)**), confirming that MgO loading enhances the

charge separation efficiency and carrier stability under illumination[36]. EIS further corroborates the enhanced charge transfer in MgO(200)@g-C_3N_4, as evidenced by its smaller Nyquist plot radius (**Fig. 3(h)**)[37]. The open-circuit potential (OCP) curve is shown in **Fig. 3(i)**. After the addition of PMS, the potential increased sharply and then reached equilibrium, indicating that the PMS molecules were rapidly adsorbed onto the catalyst surface[38]. During this process, some electrons were transferred from the catalyst to the PMS molecules, forming a metastable intermediate (catalyst-PMS*) that elevated the oxidation potential of the catalysts. MgO(200)@g-C_3N_4 exhibits a greater increase in OCP than g-C_3N_4, demonstrating its superior PMS adsorption capacity.

3.3. Degradation performance of the photocatalysts

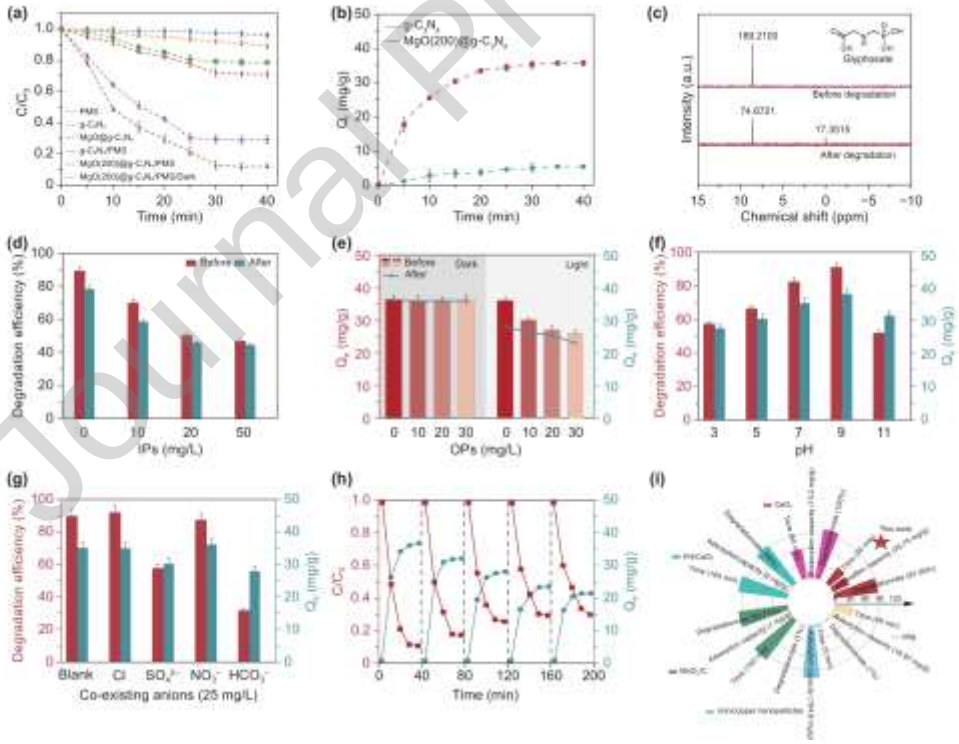


Fig. 4. (a) Degradation of glyphosate in various systems; (b) IP adsorption capacities of g-C_3N_4 and MgO(200)@g-C_3N_4; (c) solution-state ^{31}P NMR spectra of glyphosate before and after degradation; (d) glyphosate degradation efficiency under different IP concentrations; (e) IP adsorption in the presence of glyphosate under dark and light conditions (Before: fresh catalyst; After: regenerated catalyst); (f) IP adsorption capacity and glyphosate degradation efficiency by MgO(200)@g-C_3N_4 under various

pH conditions; (g) effects of coexisting anions on glyphosate degradation and IP adsorption; (h) cycling performance for glyphosate degradation and IP adsorption; (i) comparison of glyphosate degradation efficiency and IP adsorption capacity between the as-prepared catalyst and recently reported catalysts.

The removal of glyphosate in various aqueous systems was evaluated, and the results are shown in **Fig. 4(a)**. The adsorption of glyphosate onto g-C_3N_4 and MgO(200)@g-C_3N_4 was negligible (**Fig. S3**). Without a catalyst, PMS alone could not degrade glyphosate. In the absence of PMS, the glyphosate degradation rates of g-C_3N_4 and MgO(200)@g-C_3N_4 were 22% and 27%, respectively. In the presence of PMS, the degradation efficiencies increased to 70.9% and 87.9%, respectively, indicating that both catalysts can activate PMS to generate reactive oxygen species (ROS) for glyphosate degradation. The MgO(200)@g-C_3N_4/PMS system achieved only 11.1% glyphosate degradation in the dark, which is far below the 87.9% achieved under visible light, confirming that light irradiation is essential for efficient PMS activation. The MgO(200)@g-C_3N_4/PMS system exhibited a degradation efficiency 3.26 times higher than that of MgO(200)@g-C_3N_4 alone and 1.24 times higher than that of the g-C_3N_4/PMS system, demonstrating that the synergy between MgO and g-C_3N_4 significantly enhances the catalytic performance. Based on pseudo-first-order kinetic analysis (**Fig. S4**), the MgO(200)@g-C_3N_4/PMS system achieved the highest reaction-rate constant (0.0579 min^{-1}), which was 6.16 times that of MgO(200)@g-C_3N_4 alone and 1.70 times that of the g-C_3N_4/PMS system, further confirming the superior catalytic activity of the composite in activating PMS. During the degradation process, OPs were progressively oxidized and ultimately mineralized into IPs.

To assess the potential environmental impact of IPs, the IP adsorption behaviors of g-C_3N_4 and MgO(200)@g-C_3N_4 were further investigated. As shown in **Fig. 4(b)**, at the 40-min adsorption equilibrium, the adsorption capacity of g-C_3N_4 for IPs was only 5.40 mg/g, indicating its limited adsorption ability. In contrast, the adsorption capacity of MgO(200)@g-C_3N_4 for IPs reached 35.75 mg/g, which is significantly higher than that of g-C_3N_4. In addition, as shown in **Fig. S5**, the equilibrium adsorption capacity increased significantly with increasing concentration. The calculated maximum IP adsorption capacities of g-C_3N_4 and MgO(200)@g-C_3N_4 were 11.00 and 47.89 mg/g, respectively.

Complexation between the IPs and MgO was confirmed using multiple characterization techniques. SEM images (**Fig. S6a**) show that MgO(200)@g-C_3N_4 maintains its tubular framework after phosphorus adsorption, with phosphorus uniformly distributed across the material surface, indicating efficient chemisorption via Mg–O–P bonding and surface migration. Furthermore, XRD patterns (**Fig. S6b**) reveal a decrease in the characteristic MgO peaks and the emergence of diffraction peaks corresponding to $Mg_3(PO_4)_2$ and $Mg(H_2PO_4)_2$. This result indicates that MgO(200)@g-C_3N_4 can effectively capture and stabilize IPs. FTIR further confirms this mechanism with the appearance of new peaks at 1068 cm^{-1} (P–O stretching vibration) and 588 cm^{-1} (Mg–O–P vibration) (**Fig. S6c**), indicating the formation of chemical bonds between the IPs and MgO sites. The XPS analysis provides direct evidence through the P 2p spectrum (**Fig. S6d**), which identifies three magnesium-bound phosphate species, and the Mg 1s spectrum (**Fig. S6e**) shows a binding energy shift to 1304.9 eV alongside a

new peak at 1304.3 eV, corresponding to electron transfer in the Mg–O–P bonds and the formation of Mg–P bonds. These results demonstrate that MgO acts as the main active site for the chemical adsorption of IPs through Mg–O–P coordination, whereas g-C_3N_4 serves as a stable carrier. **Fig. S7** demonstrates that glyphosate can be converted into IPs, with MgO(200)@g-C_3N_4 exhibiting the highest conversion ratio, and this composite achieves efficient recovery of the converted IPs, with a recovery ratio of approximately 84.3%.

Fig. 4(c) shows the ^{31}P NMR spectra of glyphosate solutions before and after degradation[39]. The spectra show that only monoester phosphorus can be clearly identified in the original glyphosate solution. After the photocatalytic treatment of glyphosate with MgO(200)@g-C_3N_4/PMS, the peak intensity of phosphate increased, whereas that of monoester phosphorus decreased. This observation confirms that glyphosate was successfully degraded into IPs.

The catalytic adsorption synergy of MgO(200)@g-C_3N_4 was systematically evaluated in coexisting OP/IP systems, revealing competitive site occupation and irreversible deactivation mechanisms. The effect of varying the IP concentration on OP degradation is shown in **Fig. 4(d)**. As the IP (KH_2PO_4) concentration increased from 0 to 50 mg/L, the OP degradation rate decreased from 89.3% to 46.8%, demonstrating the significant inhibitory effect of IPs on catalytic activity. In the low-concentration range (0–10 mg/L), the degradation rate sharply declined by 19.2%, which is attributed to the rapid occupation of the MgO active sites by IPs through electrostatic adsorption and coordination exchange, substantially hindering OP access to the active sites. When the

Journal Pre-proof

IP concentration was increased to 20–50 mg/L, the degradation rate decreased by only 3.5% and then stabilized, indicating near-saturation of the active sites on the catalyst surface and equilibrium of the shielding effect.

After regeneration via ultrasonic desorption (using 0.1 mol/L NaOH solution as the desorption solvent, ultrasonic power: 100 W, ultrasonic treatment time: 30 min), the degradation efficiency of the catalyst decreased at all concentrations, but the extent of reduction exhibited concentration dependence. In the low-concentration range (0–10 mg/L), the degradation rate decreased by 11.8% after regeneration, primarily because the IPs were mainly physically adsorbed at low concentrations. Although ultrasonic treatment removed most of the adsorbed IPs, residual species still blocked some active sites. In the high-concentration range (20–50 mg/L), the degradation rate showed minimal change (45.6%–44.2%) and remained stable after regeneration, suggesting strong binding between the IPs and the catalyst surface at high concentrations, which prevented complete removal even with ultrasonic desorption. The remaining IPs continuously shielded the active sites, resulting in a small decrease in the degradation rate.

In addition, dual-mode dark adsorption and photocatalysis experiments were conducted on the IPs under different OP concentration gradients (simultaneous catalysis and adsorption). As shown in **Fig. 4(e)**, under dark adsorption conditions, the IP adsorption capacity remained stable at 35.7–36.3 mg/g, unaffected by OP concentration, and the adsorption performance was fully restored after regeneration, indicating reliance on inherently stable chemical adsorption sites of the material. In contrast, under

photocatalytic–adsorption synergy, the IP adsorption capacity decreased to 26.1 mg/g with increasing OP concentration, attributable to competitive adsorption among the original IPs, intermediates (including small organic acids), and final IPs generated during glyphosate photocatalytic degradation. The competitive effect was weaker at low OP concentrations; at high concentrations, the competitive effect was stronger but its rate of increase slowed owing to the near-saturation of adsorption sites.

After regeneration, the IP adsorption capacity in the photocatalytic group further declined, with a more pronounced reduction than that in the dark adsorption group, and exhibited a steeper decreasing trend as the concentration increased. This trend indicates that the strong adsorption of intermediates during photocatalysis causes irreversible deactivation of some active sites, making it difficult to restore the IP adsorption performance of MgO(200)@g-C_3N_4 after regeneration.

Fig. 4(f) shows the glyphosate degradation and IP adsorption properties of MgO(200)@g-C_3N_4 under different pH conditions[40]. The results reveal that under acidic conditions, H^+ competes for adsorption sites and inhibits PMS activation, leading to poor system performance. Within the neutral to weakly alkaline range, the catalyst maintains a stable interfacial structure and achieves synergistic optimization of catalysis and adsorption, with optimal performance at pH 9.0. In strongly alkaline environments, radical quenching and ion competition cause an obvious decline in performance. The optimal applicable pH range of 7.0–9.0 effectively solves the pH incompatibility between PMS activation and MgO adsorption, making the system suitable for natural water environments.

Other anions, such as Cl^-, SO_4^{2-}, NO_3^- and HCO_3^-, also exist in wastewater, which may affect the degradation efficiency of glyphosate and the adsorption capacity of IPs. As shown in **Fig. 4(g)**, Cl^- promotes the degradation of glyphosate, with a degradation efficiency of 91.7%. The oxidation of Cl^- by PMS forms HOCl/Cl_2, whose strong oxidizing capability enhances glyphosate degradation[1]. NO_3^- has a very small inhibitory effect on the degradation of glyphosate. The active nitrate radical (NO_3•) generated from NO_3^- can still contribute to the oxidation of OPs, despite its relatively lower oxidation potential (2.0–2.2 V) compared to hydroxyl radicals, resulting in only a minor inhibitory effect. In contrast, SO_4^{2-} and HCO_3^- have a strong negative effect on the degradation of glyphosate, with degradation efficiencies of 57.5% and 31.6%, respectively. SO_4^{2-} can react with free radicals (•OH), thereby consuming free radicals and reducing the degradation efficiency of glyphosate[41]. Meanwhile, HCO_3^- can quench free radicals or generate the carbonate radical (HCO_3•/CO_3•$^-$), which has a relatively weak oxidation potential, thereby reducing the reaction rate. Similarly, the presence of HCO_3^- and SO_4^{2-} leads to a significant decrease in the adsorption capacity of MgO(200)@g-C_3N_4 for IP ions.

Humic acid (HA) is natural organic matter ubiquitous in wastewater. As shown in **Fig. S8**, HA inhibits glyphosate degradation in a dose-dependent manner[42]. Simultaneously, the adsorption capacity of MgO(200)@g-C_3N_4 for IPs decreases with increasing HA concentration. These trends hold because the functional groups (e.g., carboxyl and hydroxyl) in humic acid compete with glyphosate for the active sites on the catalyst surface. Furthermore, HA molecules can wrap around the catalyst or form

complexes with glyphosate, thereby concurrently reducing both the glyphosate degradation efficiency and the adsorption capacity for IPs.

Cyclic stability tests were conducted to evaluate the reusability and stability of MgO(200)@g-C_3N_4. As shown in **Fig. 4(h)**, MgO(200)@g-C_3N_4 exhibits excellent stability, with a glyphosate degradation efficiency of 68.9% after five test cycles. The adsorption capacity for the IPs was maintained at 20.51 mg/g. The structural stability of MgO(200)@g-C_3N_4 was further evaluated by SEM, XRD, FTIR, and XPS. After multiple degradation and adsorption cycles, the morphology of MgO(200)@g-C_3N_4 became rougher than that in the initial state (**Fig. S9a**). Elemental mapping (**Fig. S9b**) shows a uniform distribution of C and N, with obvious agglomeration of MgO particles and the possible attachment of small amounts of amorphous substances. The XRD results (**Fig. S9c**) show that the characteristic peak of $Mg_3(PO_4)_2$ was detected in MgO(200)@g-C_3N_4 after five cycles, suggesting the crystallization and deposition of IPs on the catalyst surface. However, the main peak did not shift, indicating that the framework remains stable.

A comparison of the infrared spectra before and after five cycles (**Fig. S9d**) shows that the peak positions, shapes, and relative intensities of the characteristic functional groups are virtually identical. Therefore, the chemical structure and surface properties of the catalyst are maintained after repeated catalytic, adsorption, desorption, and regeneration cycles. **Fig. S9e,f** shows that the electronic structure of N 1s in MgO(200)@g-C_3N_4 did not change significantly after cycling. A new peak appeared at 1304.6 eV in the Mg 1s XPS spectrum, which is directly attributed to the Mg–P bond.

Journal Pre-proof

The presence of this peak confirms that glyphosate was gradually oxidized and mineralized to IPs, which were ultimately adsorbed by the MgO active sites of the MgO(200)@g-C_3N_4 catalyst. The core active site structure was stable, demonstrating the good cycling stability of MgO(200)@g-C_3N_4.

As shown in **Fig. 4(i)**, several recently developed catalysts have demonstrated specific potential for either IP adsorption or glyphosate degradation[6,43,44]. For instance, CeO_2 has performed exceptionally well in degradation because of its abundant oxygen vacancies, whereas single iron/copper nanoparticles have excelled in adsorption. However, these materials typically perform a single function. The core advantage of the MgO(200)@g-C_3N_4 material developed in this study lies in its outstanding synergy, which successfully integrates high phosphorus adsorption capacity with efficient glyphosate degradation. This catalytic–adsorption synergy enables MgO(200)@g-C_3N_4 to achieve a performance that surpasses that of most previously reported catalysts.

3.4. Photocatalytic mechanism research and pathways of glyphosate degradation

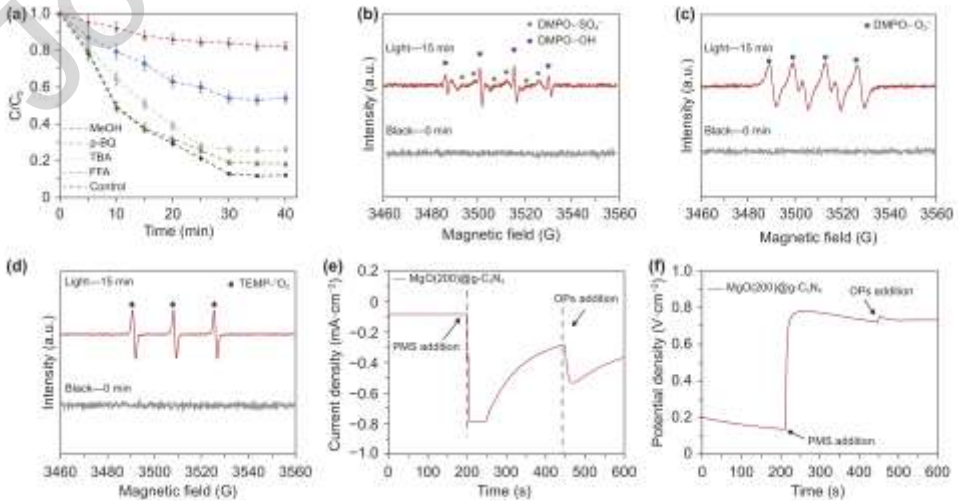


Fig. 5. (a) Plot of degradation ratio of glyphosate with additions of scavengers over MgO(200)@g-C_3N_4/PMS; (b) EPR spectra of DMPO-•OH and DMPO-$SO_4^{\bullet-}$; (c) EPR

spectra of DMPO-•O^{2-}; (d) EPR spectra of TEMP-$^1O_2$; (e) current responses after the sequential injection of PMS and glyphosate at different working electrodes; (f) open-circuit potential of MgO(200)@g-C_3N_4.

To investigate the reaction pathways and mechanisms, radical scavenging experiments were conducted to determine the types of ROS generated in the MgO(200)@g-C_3N_4/PMS system. Radical scavengers, including *tert*-butyl alcohol (TBA, the probe for •OH), methanol (MeOH, the probe for •OH and $SO_4^{\bullet-}$), p-benzoquinone (p-BQ, the probe for $\bullet O_2^-$), and furfuryl alcohol (FFA, the probe for $^1O_2$), were used to investigate the presence of various ROS[34,45]. As shown in **Fig. 5(a)**, the presence of FFA had almost no effect, indicating that $^1O_2$ played a negligible role in this process. The addition of TBA had a minor impact on glyphosate degradation, with approximately 76% of the glyphosate eliminated, suggesting that hydroxyl radicals contributed weakly to glyphosate degradation. The removal of glyphosate was inhibited to 46% and 18% after the addition of p-BQ and MeOH, respectively, indicating that $\bullet O_2^-$ and $SO_4^{\bullet-}$ played dominant roles in glyphosate degradation.

Using DMPO and TEMP as spin-trapping reagents, the ROS species were further characterized using electron paramagnetic resonance (EPR). As shown in **Fig. 5(b–d)**, under dark conditions, the EPR signals of DMPO-•OH, DMPO-$SO_4^{\bullet-}$, DMPO-$\bullet O_2^-$, and TEMP-$^1O_2$ were almost undetectable. However, under light conditions, the characteristic peaks of DMPO-$SO_4^{\bullet-}$ (1:1:1:1:1:1), DMPO-•OH (1:2:2:1), and DMPO-$\bullet O_2^-$ (1:1:1:1) were detected. Similarly, the typical three-line spectrum of TEMP-$^1O_2$ was clearly detected, indicating that •OH, $\bullet O_2^-$, $^1O_2$, and $SO_4^{\bullet-}$ were generated in the MgO(200)@g-C_3N_4/PMS system. The results of the EPR test were highly consistent

with those of the quenching experiments, suggesting that $\bullet O_2^-$ and sulfate radicals were the main causes of glyphosate degradation.

The electron transfer between MgO(200)@g-C_3N_4, PMS, and glyphosate molecules was evaluated using chronoamperometry (*i–t* curve, **Fig. 5(e)**)[46]. When PMS was added to the system at 200 s, the negative current increased rapidly from 0 to 0.97 mA cm^{-2}, indicating that the addition of PMS significantly affected the current output. The MgO(200)@g-C_3N_4 catalyst surface provided electrons to PMS, resulting in a sharp increase in the current. Subsequently, the introduction of glyphosate at 450 s caused a second surge in the negative current, indicating electron transfer from the glyphosate molecules (donor) to PMS (acceptor), with MgO(200)@g-C_3N_4 serving as an electron-transfer mediator.

In addition, the open-circuit potential was monitored to verify whether glyphosate degraded via a catalyst-mediated electron-transfer mechanism[47]. As shown in **Fig. 5(f)**, after the addition of PMS, the open-circuit potential of the glassy carbon electrode coated with MgO(200)@g-C_3N_4 immediately increased due to the consumption of electrons on the catalyst surface by PMS, which decreased the interfacial electron concentration and increased the redox potential. After the addition of glyphosate, the open-circuit potential shifted slightly in the positive direction. Glyphosate provided electrons to the catalyst, but at the same time, PMS* rapidly consumed electrons to generate free radicals, accelerating the overall rate of electron transfer. The interfacial electron concentration fluctuated briefly, but the open-circuit potential maintained a slightly positive shift. Chronoamperometry (*i–t* curve) and open-circuit potential

monitoring indicated that MgO(200)@g-C_3N_4 served as an electron-transfer mediator, achieving efficient catalytic degradation of glyphosate by mediating electron transfer between PMS and glyphosate.

3.5. Practical experiment and toxicity assessment

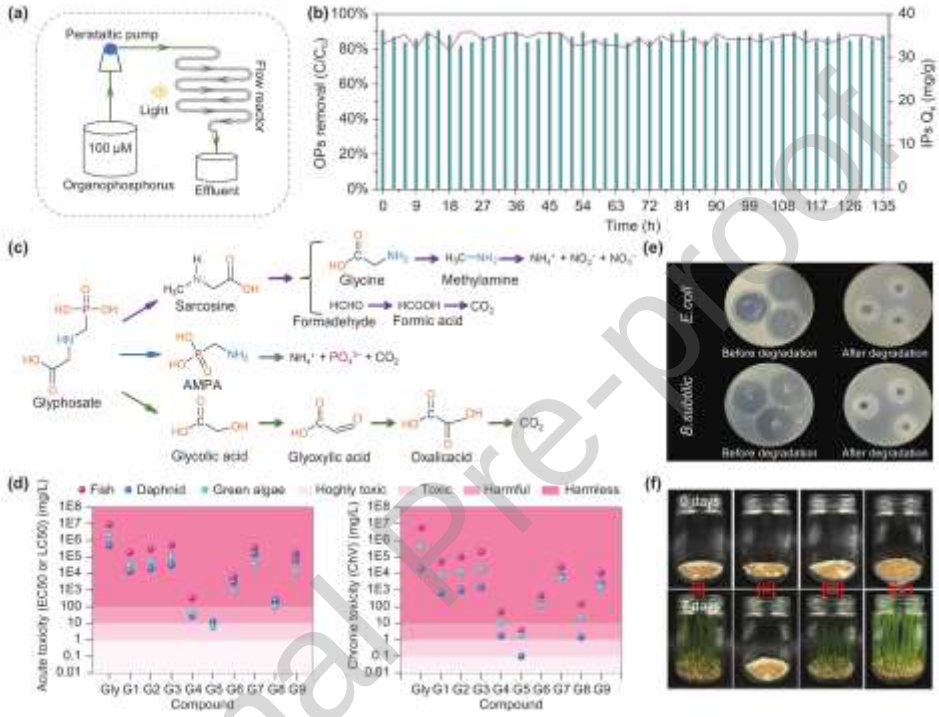


Fig. 6. (a) Schematic of the continuous flow system; (b) removal of OPs and adsorption capacity of IPs; (c) proposed oxidation pathways of glyphosate; (d) toxicity prediction of glyphosate and its metabolic intermediates: (I) acute toxicity and (II) chronic toxicity; (e) toxicity tests using *B. subtilis* and *E. coli* as biological indicators, showing the size of the inhibition ring; (f) phenotype of representative wheat seeds treated with different solutions for 7 days: (I) water (control), (II) glyphosate aqueous solution, (III) degraded glyphosate aqueous solution, (IV) IP aqueous solution.

To evaluate the practical potential of MgO(200)@g-C_3N_4 for activating PMS in the treatment of phosphorus-spiked natural water samples, a continuous-flow reaction system was constructed (**Fig. 6(a)**)[38]. The system employed an S-shaped raceway reactor to continuously treat the wastewater (spiked with 100 μM glyphosate) under visible-light irradiation with a hydraulic retention time of 30 min. **Fig. 6(b)** shows that,

during 135 h of continuous operation, the OP removal rate remained stable at approximately 90%, whereas the IP adsorption capacity was maintained at 32–35 mg/g. These results demonstrate the sustained and efficient purification capability of the system for phosphorus-containing pollutants, indicating its potential for practical applications. The glyphosate concentration decreased continuously over the reaction period, whereas its key degradation intermediate, AMPA, exhibited a typical rise-and-fall profile, peaking at 20 min before gradually declining. This concentration pattern clearly demonstrates the sequential conversion of glyphosate to AMPA and the subsequent degradation of the intermediate (**Fig. S10**).

To further elucidate the degradation pathway of glyphosate, the intermediates were identified by HPLC-MS, and three proposed pathways are depicted in **Fig. 6(c).** The glyphosate molecule was adsorbed onto the MgO(200)@g-C_3N_4 surface via coordination between its phosphonic acid group and the surface Mg^{2+} sites. Under visible-light irradiation, MgO(200)@g-C_3N_4 acted as an electron-transfer medium to activate PMS, generating ROS that drive three degradation pathways. Pathway I proceeds via cleavage of the C–N bond adjacent to the carboxyl group, yielding sarcosine, which sequentially degrades into glycine, methylamine, formaldehyde, and other small intermediates, ultimately mineralizing to NH_4^+, NO_2^-, NO_3^-, and CO_2. Pathway II involves cleavage of the C–N bond adjacent to the phosphonic group to form AMPA, which is further oxidized to inorganic phosphate and inorganic nitrogen species. This result is consistent with the ^{31}P NMR data. Pathway III arises from radical attack on the C–P bond and carbon skeleton, generating small-molecule carboxylic

acids (glycolic, glyoxylic, and oxalic acids) alongside phosphorus-containing intermediates such as H_3PO_3. All these intermediates are eventually fully oxidized to CO_2, H_2O, and PO_4^{3-}.[48].

The ECOSAR program was used to evaluate the toxicity risks of glyphosate (Gly) and its degradation intermediates in three aquatic organisms (fish, Daphnia, and green algae)[49]. As shown in **Fig. 6(d)** and **Table 2**, the acute toxicity values of the parent glyphosate for the three types of organisms are 9,140,000, 49,600, and 1,940,000 mg/L, respectively, and the chronic toxicity values are 5,860,000, 18,900, and 365,000 mg/L, respectively. Although the toxicity is relatively low, a potential ecological risk still exists.

The degradation products can be classified into two categories based on their toxicity: a low-toxicity group (G1, G2, G3, G6, G7, and G9), whose toxicity is enhanced compared to that of the parent compound but remains low , and a moderately toxic group comprising G5, which has acute and chronic toxicity to all three types of organisms, and G4, which is toxic to water fleas and green algae. The residual toxicity of these two products stems from the fact that the amino group of methylamine (G4) is prone to reacting with biological macromolecules, and the high reactivity of formaldehyde (G5) can induce protein–nucleic acid cross-linking. Moreover, both G4 and G5 exhibit strong metabolic accumulation and the capacity to interfere with cellular physiology.

This study reveals that the photocatalytic degradation process involves competing pathways for toxicity enhancement and detoxification. Accordingly, the efficient

conversion of OPs into IPs via gradual oxidation is critical for reducing the toxicity of the reaction system. Given the risk of generating toxic intermediates, such as G4 and G5, the overall effluent toxicity was systematically assessed in subsequent bioassays.

Antibacterial experiments were conducted using *Bacillus subtilis* and *Escherichia coli* as test strains, with the diameter of the inhibition zone as the evaluation indicator: a larger inhibition zone indicates a stronger inhibitory effect on bacterial growth and higher toxicity[50]. As shown in **Fig. 6(e)** and **Fig. S11**, the diameters of the inhibition zones of glyphosate before degradation were 33.0 mm for *E. coli* and 37.0 mm for *B. subtilis*. After degradation, the diameter of the inhibition zone for *E. coli* decreased to 9.0 mm (a reduction of 72.7%), and for *B. subtilis*, it decreased to 11.0 mm (a reduction of 70.3%). Compared to those before degradation, the inhibition zone diameters after degradation were significantly reduced for both *E. coli* and *B. subtilis*. Thus, following degradation, the toxicity of glyphosate toward both test strains was greatly reduced, indicating that the degradation process effectively weakened the toxicity of glyphosate, exhibiting a detoxification effect.

The toxicity of the effluent from the continuous-flow treatment system toward plants was evaluated using a wheat-seed germination experiment[51]. Seedlings were exposed to deionized water, glyphosate solution, glyphosate solution after degradation, or an IP buffer solution. The inhibitory effects were significantly different among groups. As shown in **Fig. 6(f)** and **Fig. S12**, after 7 days of cultivation, the deionized water group (I) germinated normally, with a germination rate of 92% and an average stem length of 7.5 cm; the glyphosate group (II) experienced completely inhibited

germination, confirming the strong phytotoxicity of glyphosate; and the degradation group (III) had significantly reduced toxicity, with a germination rate of 81% and a stem length of 6.6 cm, indicating that the system effectively degraded glyphosate and weakened the inhibitory effect. The IP buffer solution group (IV) showed enhanced seedling growth compared to group (V) (Water control), with a germination rate of 93% and stem length of 8.6 cm, suggesting that IPs are non-toxic and may act as nutrients to promote growth. The control group (VI) excluded the influence of residual PMS (**Fig. S13**). In conclusion, the MgO(200)@g-C_3N_4/PMS system degraded glyphosate in an environmentally friendly manner, effectively removing pollutants and significantly reducing its ecological toxicity.

4. Conclusions

In this study, we successfully developed a bifunctional MgO(200)@g-C_3N_4 catalyst with capabilities for both catalytic degradation and adsorptive recovery, enabling the integrated treatment of OP-containing wastewater. Under visible-light ($\lambda \geq 420$ nm) irradiation, the system achieved a degradation rate of 87.9% for OPs and an adsorption capacity of 35.75 mg/g for IPs, effectively realizing the synergistic transformation of OP degradation and IP fixation. The material demonstrated excellent stability and adaptability after five cycles and in different water-quality matrices. Multi-mode mechanistic studies, including EPR, radical-quenching experiments, and electrochemical tests, revealed the generation and action mechanism of ROS in the MgO(200)@g-C_3N_4/PMS system: g-C_3N_4 mediates the electron transfer between glyphosate and PMS, simultaneously activating PMS to generate ROS, mainly

composed of $SO_4^{\bullet-}$ and $\bullet O_2^-$, that convert glyphosate into IPs. MgO(200) utilizes its high-density Mg^{2+} sites to form a Mg–O–P coordination structure with PO_4^{3-}, achieving in-situ fixation of IPs. The synergistic catalysis–adsorption technology developed in this study can achieve the dual goals of efficient pollutant degradation and phosphorus resource recovery, providing key technical support for the transformation of wastewater treatment from simple purification to a pollution control–resource recovery model.

Declaration of Competing Interest

The authors declare that they have no known competing financial interests or personal relationships that could have appeared to influence the work reported in this paper.

Acknowledgements

This work was financially supported by the Science and Technology Planning Project (2024DA052), the Science and Technology Program - Regional Innovation Guidance Program (2023ZD080), the Tianchi Talent Project (CZ002735(3123), BT2025TCYC0060), the National Natural Science Foundation of China (22408237, 32541085), the Research Initiation Project of Shihezi University (RCZK202330), the Science and Technology Group of Xi'an Polytechnic University that Assists the Urumqi Project (HSYCP2025-018), and the Ministry of Science and Higher Education of the Russian Federation (1240122001838).

Journal Pre-proof

References

[1] R.R. Zhao, H.L. Liu, D. Chen, D. Huang, C.J. Zhang, H.Y. Shi, J.X. Yu, R.P. Li, Y.P. Huang, Selective C−P bond cleavage in glyphosate degradation via singlet oxygen-dominated alkali-activated peroxymonosulfate, J. Hazard. Mater. 496 (2025) 139330.

[2] M.J. Qu, L.T. Wang, Q. Xu, J.Q. An, Y.J. Mei, G.L. Liu, Influence of glyphosate and its metabolite aminomethylphosphonic acid on aquatic plants in different ecological niches, Ecotoxicol. Environ. Saf. 246 (2022) 114155.

[3] N. Tresnakova, A. Stara, J. Velisek, Effects of glyphosate and its metabolite AMPA on aquatic organisms, Appl. Sci. 11 (2021) 9004.

[4] H.M. Azam, S.T. Alam, M. Hasan, D.D.S. Yameogo, A.D. Kannan, A. Rahman, M.J. Kwon, Phosphorous in the environment: Characteristics with distribution and effects, removal mechanisms, treatment technologies, and factors affecting recovery as minerals in natural and engineered systems, Environ Sci Pollut Res 26 (2019) 20183–20207.

[5] C. Xing, J. Shi, F.M. Cui, J.C. Shen, H. Li, Fe^{2+}/H_2O_2-strengite method with the enhanced settlement for phosphorus removal and recovery from pharmaceutical effluents, Chemosphere 277 (2021) 130343.

[6] M. Wang, G.L. Zhang, G.N. Qiu, D.Q. Cai, Z.Y. Wu, Degradation of herbicide (glyphosate) using sunlight-sensitive MnO_2/C catalyst immediately fabricated by high energy electron beam, Chem. Eng. J. 306 (2016) 693–703.

[7] M. Russo, G. Iervolino, V. Vaiano, W-doped ZnO photocatalyst for the degradation of glyphosate in aqueous solution, Catalysts 11 (2021) 234.

[8] Y.Y. Ahn, E.T. Yun, J.W. Seo, C. Lee, S.H. Kim, J.H. Kim, J. Lee, Activation of Peroxymonosulfate by Surface-Loaded Noble Metal Nanoparticles for Oxidative Degradation of Organic Compounds, Environ. Sci. Technol. 50 (2016) 10187–10197.

[9] Y.J. Li, J. Li, Y.T. Pan, Z.K. Xiong, G. Yao, R.Z. Xie, B. Lai, Peroxymonosulfate activation on $FeCo_2S_4$ modified g-C_3N_4 ($FeCo_2S_4$-CN): Mechanism of singlet oxygen evolution for nonradical efficient degradation of sulfamethoxazole, Chem. Eng. J. 384 (2020) 123361.

[10] W.C. Xu, H.S. Guan, Z. Liu, X.D. Jiang, X.L. Wu, B. Ruan, Y.H. Sun, X.F. Li, H.L. Wang, K.L. Yeung, Enhanced peroxymonosulfate activation by ball-milling-assisted nitrogen-doped

animal-derived biochar for sulfamethoxazole degradation: Unveiling multiple non-radical mechanisms, Sep. Purif. Technol. 373 (2025) 133570.

[11] Z.Z. Zhu, Z. Li, X.X. Wei, J.J. Wang, S.H. Xiao, R. Li, R. Wu, J.S. Chen, Achieving efficient electroreduction of CO_2 to CO in a wide potential window by encapsulating ni nanoparticles in N-doped carbon nanotubes, Carbon 185 (2021) 9–16.

[12] W.J. Cheng, H. Liu, G.F. Liao, R.J. Wang, X.M. Zhao, L.M. Zhou, R.D. Rodriguez, B. Yang, X. Jia, Directional charge transfer modulation in ultrathin polyporous carbon nitride nanotubes for enhanced peroxymonosulfate activation, Carbon 222 (2024) 118977.

[13] L. Jin, Y.P. Huang, L.Q. Ye, X. Liu, D. Huang, Revealing the vital role of dissolved O_2 in Cu(II)-Cu(I)-Cu(III) cycle for promoting glyphosate degradation via percarbonate activation, Sep. Purif. Technol. 353 (2025) 128304.

[14] R.D. Wang, X.Y. Huang, Y. Wang, Y.Q. Chen, X.B. Xu, S.S. Deng, Z.L. Yin, Y. Dai, W. Yang, Adsorption of phosphate and glyphosate by MOFs modified Resin: The role of metal centers and organic linkers, Chem. Eng. J. 507 (2025) 160792.

[15] Z.L. Li, X. Liu, J.Y. Yan, Y.Z. Wang, R.P. Li, Y.P. Huang, S.B. Wang, D. Huang, Catalytic wastewater dephosphorization for phosphorus recycling to fertilizers, Appl. Catal. B: Environ. Energy 369 (2025) 125154.

[16] P.L. Gao, Y.C. Zhang, S.F. Wang, Increasing the hydrophyte removal rate of dissolved inorganic phosphorus using a novel Fe-Mg-loaded activated carbon hydroponic substrate with adsorption-release dual functions, J. Environ. Manag. 313 (2022) 114998.

[17] T. Yuan, S.Y. Lv, X.Y. Zhang, Y.H. Luo, M.L. Feng, W.L. Fu, P. Yang, K.R. Fu, Y.L. Luo, Y.Z. Cao, F. Wang, Efficient recovery of high-concentration phosphorus from livestock wastewater: Combined effects of magnesium-based metal-organic framework-derived metal oxide morphology and magnesium oxide different vacancie species, Sep. Purif. Technol. 374 (2025) 133784.

[18] Y. Cheng, Q. Xie, Z.D. Wu, L. Ji, Y.F. Li, Y.J. Cai, P.K. Jiang, B. Yu, Mechanistic insights into the selective adsorption of phosphorus from wastewater by MgO(100)-functionalized cellulose sponge, Sci. Total Environ. 868 (2023) 161646.

[19] J.B. Zhou, S.L. Yang, J.G. Yu, Facile fabrication of mesoporous MgO microspheres and their

enhanced adsorption performance for phosphate from aqueous solutions, Colloids Surf. A: Physicochem. Eng. Aspects 379 (2011) 102–108.

[20] K. Ooi, A. Sonoda, Y. Makita, M. Torimura, Comparative study on phosphate adsorption by inorganic and organic adsorbents from a diluted solution, J. Environ. Chem. Eng. 5 (2017) 3181–3189.

[21] Q.R. Zhang, Z.X. Zhang, J. Teng, H.M. Huang, Q.M. Peng, T.F. Jiao, L. Hou, B. Li, Highly efficient phosphate sequestration in aqueous solutions using nanomagnesium hydroxide modified polystyrene materials, Ind. Eng. Chem. Res. 54 (2015) 2940–2949.

[22] T.Y. Li, L.F. Ge, X.X. Peng, W.Z. Wang, W. Zhang, Enhanced degradation of sulfamethoxazole by a novel Fenton-like system with significantly reduced consumption of H_2O_2 activated by g-C_3N_4/MgO composite, Water Res. 190 (2021) 116777.

[23] L. Jia, X.X. Cheng, X.N. Wang, H. Cai, P. He, J.Y. Ma, L.L. Li, Y. Ding, X.X. Fan, Large-Scale Preparation of g-C_3N_4 Porous Nanotubes with Enhanced Photocatalytic Activity by Using Salicylic Acid and Melamine, Ind. Eng. Chem. Res. 59 (2020) 1065–1072.

[24] J.L. Sun, H.Z. Wu, C.H. Fu, C.H. Zhang, Z.Z. Hu, M.H. Zhou, Novel Fenton-like system based on bifunctional MgO/g-C_3N_4 S-scheme heterojunction photoanode for efficient tetracycline degradation, Appl. Catal. B: Environ. and Energy 351 (2024) 123976.

[25] L.F. Ge, Y.M. Yue, W. Wang, F.T. Tan, S.H. Zhang, X.Y. Wang, X.L. Qiao, P.K. Wong, Efficient degradation of tetracycline in wide pH range using MgNCN/MgO nanocomposites as novel H_2O_2 activator, Water Res. 198 (2021) 117149.

[26] Y. Wu, J. Chen, H.N. Che, X. Gao, Y.H. Ao, P. Wang, Boosting $2e^-$ oxygen reduction reaction in garland carbon nitride with carbon defects for high-efficient photocatalysis-self-fenton degradation of 2,4-dichlorophenol, Appl. Catal. B: Environ. 307 (2022) 121185.

[27] N. Mao, J.X. Jiang, MgO/g-C_3N_4 nanocomposites as efficient water splitting photocatalysts under visible light irradiation, Appl. Surf. Sci. 476 (2019) 144–150.

[28] Z. Mo, X.M. Zhu, Z.F. Jiang, Y.H. Song, D.B. Liu, H.P. Li, X.F. Yang, Y.B. She, Y. Lei, S. Yuan, H. Li, L. Song, Q. Yan, H. Xu, Porous nitrogen-rich g-C_3N_4 nanotubes for efficient photocatalytic CO2 reduction, Appl. Catal. B: Environ. 256 (2019) 117854.

[29] A. Modwi, L. Khezami, M.G. Ghoniem, P. Nguyen-Tri, O. Baaloudj, A. Guesmi, F.K.

AlGethami, M.S. Amer, A.A. Assadi, Superior removal of dyes by mesoporous MgO/g-C_3N_4 fabricated through ultrasound method: Adsorption mechanism and process modeling, Environ. Res.205 (2022) 112543.

[30] Q. Li, Y.Q. Jiao, Y.Q. Tang, J. Zhou, B.G. Wu, B.J. Jiang, H.G. Fu, Shear Stress Triggers Ultrathin-Nanosheet Carbon Nitride Assembly for Photocatalytic H_2O_2 Production Coupled with Selective Alcohol Oxidation, J. Am. Chem. Soc. 145 (2023)20837-20848.

[31] J. Miao, W. Geng, P.J.J. Alvarez, M.C. Long, 2D N-Doped Porous Carbon Derived from Polydopamine-Coated Graphitic Carbon Nitride for Efficient Nonradical Activation of Peroxymonosulfate, Environ. Sci. Technol. 54 (2020) 8473–8481.

[32] H.P. Peng, H.C. Yang, J.J. Han, X.Z. Liu, D. Su, T. Yang, S.H. Liu, C.W. Pao, Z.W. Hu, Q.B. Zhang, Y. Xu, H.B. Geng, X.Q. Huang, Defective $ZnIn_2S_4$ nanosheets for visible-light and sacrificial-agent-free H_2 O_2 photosynthesis via O_2 /H_2 O redox, J. Am. Chem. Soc. 145 (2023) 27757–27766.

[33] X.W. Ruan, S.L. Zhao, M.H. Xu, D.X. Jiao, J. Leng, G.Z. Fang, D.P. Meng, Z.F. Jiang, S.Y. Jin, X.Q. Cui, S.K. Ravi, Iso-elemental $ZnIn_2S_4$/$Zn_3In_2S_6$ heterojunction with low contact energy barrier boosts artificial photosynthesis of hydrogen peroxide, Adv. Energy Mater.14 (2024) 2401744.

[34] Y.J. Ju, Z. Wang, H.L. Lin, R.E. Hou, H. Li, Z. Wang, R.T. Zhi, X.Q. Lu, Y. Tang, F. Chen, Modulating the microenvironment of catalytic interface with functional groups for efficient photocatalytic degradation of persistent organic pollutants, Chem. Eng. J. 479 (2024) 147800.

[35] W. Wang, Z.Y. Chen, C.M. Li, B. Cheng, K. Yang, S. Zhang, G.O. Luo, J.G. Yu, S.W. Cao, Graphene quantum dot-modified $Mn_{0.2}Cd_{0.8}S$ for efficient overall photosynthesis of H_2O_2, Adv Funct Mater. 35(2025) 2422307.

[36] Z. Yang, J.L. Wang, Highly efficient photocatalytic H_2O_2 production over a $Zn_{0.3}Cd_{0.7}S$/MXene photocatalyst for degradation of emerging pollutants under visible-light irradiation, Langmuir 40 (2024) 3168–3180.

[37] D.R. Chen, C.W. Ma, Q. Zhang, C. Xue, H.N. Che, Y.H. Ao, Construction of bifunctional S-doped N-deficient carbon nitride for efficient simultaneous photocatalytic H_2O_2 synthesis and BPA degradation, Surf. Interfaces 52 (2024) 104886.

[38] B.K. Huang, X.Y. Ren, J. Zhao, Z.L. Wu, X.H. Wang, X.Y. Song, X.N. Li, B. Liu, Z.K. Xiong, B. Lai, Modulating Electronic Structure Engineering of Atomically Dispersed Cobalt Catalyst in Fenton-like Reaction for Efficient Degradation of Organic Pollutants, Environ. Sci. Technol. 57 (2023) 14071–14081.

[39] H. Li, A.F. Wallace, M.J. Sun, P. Reardon, D.P. Jaisi, Degradation of glyphosate by mn-oxide may bypass sarcosine and form glycine directly after C–N bond cleavage, Environ. Sci. Technol. 52 (2018) 1109–1117. https://doi.org/10.1021/acs.est.7b03692.

[40] L. Jin, Y.P. Huang, H.L. Liu, L.Q. Ye, X. Liu, D. Huang, Efficient treatment of actual glyphosate wastewater via non-radical fenton-like oxidation, J. Hazard. Mater. 463 (2024) 132904.

[41] Y. Xin, H.J. Wang, H. Xue, Q. Li, H.X. Li, Y. Zhang, Y.Z. Dong, H.J. Xie, Y.Y. Ma, Ti_3C_2-based MXene anchoring single-atom Co as a long-lasting peroxymonosulfate activator enabling efficient water decontamination: Deciphering the critical role of titanium vacancies, Appl. Catal. B: Environ. and Energy 365 (2025) 124966.

[42] J. Li, Z.B. Ni, Q.Z. Gao, X.X. Yang, Y.P. Fang, R.L. Qiu, M.S. Zhu, S.S. Zhang, Core-shell structured cobalt–nickel bimetallic sulfide with dual redox cycles to activate peroxymonosulfate for glyphosate removal, Chem. Eng. J. 453 (2023) 139972.

[43] H. Wu, Q. Sun, J.Y. Chen, G.Y. Wang, D. Wang, X.F. Zeng, J.X. Wang, Citric acid-assisted ultrasmall CeO_2 nanoparticles for efficient photocatalytic degradation of glyphosate, Chem. Eng. J. 425 (2021) 130640.

[44] J.W. Brockgreitens, F. Heidari, A. Abbas, Versatile process for the preparation of nanocomposite sorbents: Phosphorus and arsenic removal, Environ. Sci. Technol. 54 (2020) 9034–9043.

[45] Q.L. Ma, J.X. Wei, Z.H. Lin, Y.N. Guo, H. Tian, Q.Y. Liu, H.L. Lin, P.R. Su, Y. Tang, Enhanced photocatalytic performance of Ce^{3+}-doped $ZnIn_2S_4$ through vacancy engineering for efficient hydrogen evolution and pollutant degradation, Appl. Catal. B: Environ Energy 378 (2025) 125547.

[46] J.L. Cai, J.Q. Wan, Y. Wang, J.Y. Yi, Y.Y. Liang, Developing a β-cyclodextrin modified nanoconfined channels catalyst for efficient activation of peroxymonosulfate: Enhancing non-

radical pathways and electron transfer, Appl. Catal. B: Environ. Energy 375 (2025) 125401.

[47] X.X. Long, C.P. Feng, M. Liu, X.P. Li, Z.H. Huang, Y.X. Du, Y. Chen, S.Y. Yang, G. Wang, D.H. Ding, W.L. Huang, R.Z. Chen, PMS activation by hollow sulfur doped multilayer carbon shell wrapped CoFe alloy: Confined adsorption and surface activation, J. Cleaner Prod. 425 (2023) 138672.

[48] S.Y. Yang, F. Zhao, Y.F. Wang, J.Y. Yuan, G.J. Wang, Y.W. He, Q. Zeng, X.L. Xu, J.H. Fan, X.F. An, Engineering bifunctional biochar nanocomposites for enhanced phosphorus removal in wastewater treatment: Simultaneous organophosphorus pesticide degradation and targeted phosphate recovery through crystallization, J. Colloid Interface Sci. 698 (2025) 138015.

[49] S. Sudarshan, V.S. Bharti, S. Harikrishnan, S.P. Shukla, G. RathiBhuvaneswari, Eco-toxicological effect of a commercial dye rhodamine B on freshwater microalgae *Chlorella vulgaris*, Arch. Microbiol. 204 (2022) 658.

[50] K. Shameli, M. Bin Ahmad. M. Zargar, W.M.Z.W. Yunis, A. Rustaiyan, N.A. Ibrahim ,Synthesis of silver nanoparticles in montmorillonite and their antibacterial behavior, Int J. Nanomedicine. 6.(2011) 581-590.

[51] X.F. Sima, X.C. Shen, T. Fang, H.Q. Yu, H. Jiang, Efficiently reducing the plant growth inhibition of CuO NPs using rice husk-derived biochar: Experimental demonstration and mechanism investigation, Environ. Sci.: Nano 4 (2017) 1722–1732.

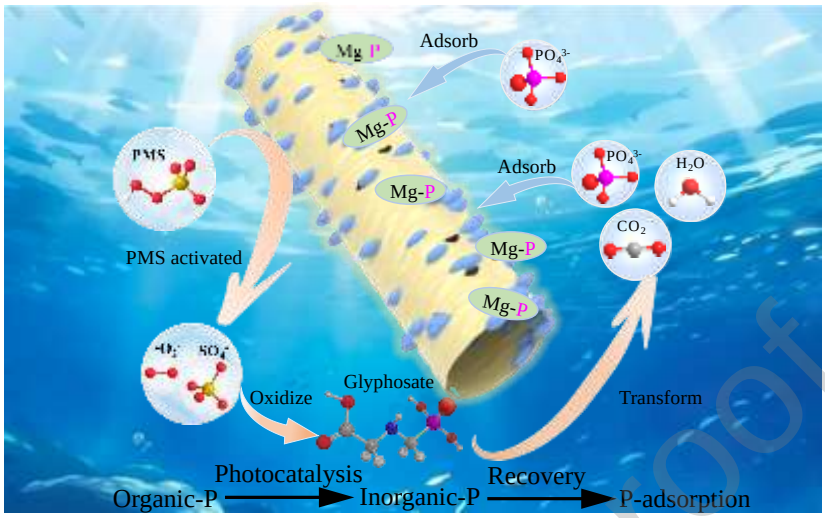
Declaration of interests

☒ The authors declare that they have no known competing financial interests or personal relationships that could have appeared to influence the work reported in this paper.

☐ The authors declare the following financial interests/personal relationships which may be considered as potential competing interests:

Journal Pre-proof

Graphic Abstract



Highlights:

1.A novel degradation-adsorption bifunctional composite catalyst was developed.

2.This sample can convert OPs into IPs and can be simultaneously recovered.

3.MgO(200)@g-C_3N_4 mediates electron transfer between glyphosate and PMS.

4.The P wastewater can serve as a P fertilizer to promote plant growth.

Journal Pre-proof